Title	A hybrid time-domain discontinuous Galerkin-boundary integral method for 3-D electromagnetic scattering analysis
Author(s)	LI, P; Shi, Y.F.; Jiang, L; Bagci, H
Citation	IEEE Transactions on Antennas and Propagation, 2014, v. 62 n. 5, p. 2841-2846
Issued Date	2014
URL	http://hdl.handle.net/10722/202839
Rights	Creative Commons: Attribution 3.0 Hong Kong License

[5] F. Ferrero, C. Luxey, G. Jacquemod, and R. Staraj, "Dual-band circularly polarized microstrip antenna for satellite applications," *IEEE Antennas Wireless Propag. Lett*, vol. 4, pp. 13–15, 2005.
[6] C. C. Chou, K. H. Lin, and H. L. Su, "Broadband circularly polarized cross-patch-loaded square slot antenna," *Electron. Lett.*, vol. 43, no. 9, pp. 485–486, Apr. 2007.
[7] J. Y. Sze, J. C. Wang, and C. C. Chang, "Axial-ratio bandwidth enhancement of asymmetric-CPW-fed circularly-polarised square slot antenna," *Electron. Lett*, vol. 44, no. 18, pp. 1048–1049, Aug. 28, 2008.
[8] S. L. S. Yang, A. A. Kishk, and K. F. Lee, "Wideband circularly polarized antenna with L-shaped slot," *IEEE Trans. Antennas Propag*, vol. 56, no. 6, pp. 1780–1783, Jun. 2008.
[9] J. Y. Sze, C. I. G. Hsu, M. H. Ho, Y. H. Ou, and M. T. Wu, "Design of circularly polarized annular-ring slot antennas fed by a double-bent microstripline," *IEEE Trans. Antennas Propag*, vol. 55, no. 11, pp. 3134–3139, Nov. 2007.
[10] C. Chen and E. K. N. Yung, "Dual-band dual-sense circularly- polarized CPW-fed slot antenna with two spiral slots loaded," *IEEE Trans. Antennas Propag*, vol. 57, no. 6, pp. 1829–1833, Jun. 2009.
[11] C. H. Chen and E. K. N. Yung, "Dual-band circularly-polarized CPW-fed slot antenna with a small frequency ratio and wide bandwidths," *IEEE Trans. Antennas Propag*, vol. 59, no. 4, pp. 1379–1384, Apr. 2011.
[12] Y. Y. Chen, Y. C. Jiao, G. Zhao, F. Zhang, Z. L. Liao, and Y. Tian, "Dual-band dual-sense circularly polarized slot antenna with a C-shaped grounded strip," *IEEE Antennas Wireless Propag. Lett*, vol. 10, pp. 915–918, 2011.
[13] C. A. Balanis, *Antenna Theory: Analysis and Design*. Hoboken, NJ, USA: Wiley, 2005, ch. 2, pp. 70–71.

A Hybrid Time-Domain Discontinuous Galerkin-Boundary Integral Method for Electromagnetic Scattering Analysis

Ping Li, Yifei Shi, Li Jun Jiang, and Hakan Bağcı

***Abstract*—A scheme hybridizing discontinuous Galerkin time-domain (DGTD) and time-domain boundary integral (TDBI) methods for accurately analyzing transient electromagnetic scattering is proposed. Radiation condition is enforced using the numerical flux on the truncation boundary. The fields required by the flux are computed using the TDBI from equivalent currents introduced on a Huygens' surface enclosing the scatterer. The hybrid DGTDBI ensures that the radiation condition is mathematically exact and the resulting computation domain is as small as possible since the truncation boundary conforms to scatterer's shape and is located very close to its surface. Locally truncated domains can also be defined around each disconnected scatterer additionally reducing the size of the overall computation domain. Numerical examples demonstrating the accuracy and versatility of the proposed method are presented.**

Manuscript received September 16, 2013; revised January 02, 2014; accepted February 02, 2014. Date of publication February 20, 2014; date of current version May 01, 2014. This work was supported in part by the Research Grants Council of Hong Kong (GRF 713011, GRF 712612, and 711511), NSFC 61271158, US AR120018, and Hong Kong UGC AoE/P–04/08.

P. Li and L. J. Jiang are with the Department of Electrical and Electronic Engineering, The University of Hong Kong, Hong Kong (e-mail: liping@eee.hku.hk; jianglj@hku.hk).

Y. Shi and H. Bağcı are with the Division of Computer, Electrical, and Mathematical Sciences and Engineering and the Center for Uncertainty Quantification in Computational Science and Engineering, King Abdullah University of Science and Technology (KAUST), Thuwal, 23955-6900, Saudi Arabia (e-mail: yifei.shi@kaust.edu.sa; hakan.bagci@kaust.edu.sa).

Color versions of one or more of the figures in this communication are available online at http://ieeexplore.ieee.org.

Digital Object Identifier 10.1109/TAP.2014.2307294

***Index Terms*—Boundary integral (BI) method, disconnected/concave scatterers, discontinuous Galerkin time-domain (DGTD) method, Huygens' principle.**

I. Introduction

Numerical analysis of transient scattering from inhomogeneous, dispersive, and/or anisotropic scatterers is indispensable in various fields of electromagnetics. Oftentimes, time-domain differential equation solvers are preferred for this purpose. However, when applied in scattering problems, these solvers require an unbounded domain to be truncated with radiation boundary conditions.

Mathematically exact absorbing boundary conditions (EACs) [1], [2] and their localized but approximate versions (ABCs) [3], [4] can be used for this purpose. EACs [1], [2] are derived from radiation conditions of outgoing wave modes but can only be enforced on planar and/or spherical boundaries. Additionally, the number of modes required for a prescribed accuracy cannot be estimated easily beforehand. Implementation of ABCs [3], [4] results in more efficient schemes but their accuracy significantly deteriorates for waves obliquely incident on the boundaries. Computation domains can also be truncated by perfectly matched layers (PMLs) [5], [6] which absorb waves incident on the truncation boundary. Although the attenuation in PML is independent of incidence angle [6], it significantly decreases at low frequencies [7], [8]. Additionally, PML-truncated differential equation solvers suffer from late time instabilities [9] as well as inaccuracies due to spurious reflections at the PML interface [5], [6]. The third approach to domain truncation is "hybridizing" the differential equation solver with the time-domain boundary integral (TDBI) method [10], [11]. This hybrid approach formulates the fields on the truncation boundary in the form of a retarded time boundary integral over a Huygens' surface that encloses the scatterer. The radiation condition enforced in this manner is mathematically exact and the resulting computation domain is as small as possible since the truncation boundary is now allowed to conform to scatterer's shape and to be located very close to its surface. Also, hybridization allows to introduce a locally truncated domains each of which is defined around a disconnected scatterer reducing significantly the size of the overall computation domain.

In this work, a discontinuous Galerkin time-domain solver (DGTD) is hybridized with the TDBI method for the first time to analyze transient electromagnetic scattering from inhomogeneous, dispersive, and/or anisotropic scatterers. The proposed hybrid DGTDBI solver posses advantages of both DGTD and TDBI methods. All DGTD spatial operations are localized and the solution is allowed to be discontinuous across boundaries between elements [12]–[17]. The information exchange among neighboring elements is facilitated via numerical flux. The mass matrix is block diagonal, where the block dimension is equal to the number of degrees of freedom in each element. These blocks are inverted and stored before time marching which results in a compact and efficient solver when combined with an explicit time integration scheme. The radiation conditions are enforced by using the incoming numerical flux on the truncation boundary. The fields required by the flux are computed using the TDBI from the equivalent electric and magnetic currents introduced on the Huygens' surface. Like the EAC-truncated DGTD methods, the resulting proposed DGTDBI solver enforces the radiation condition exactly but is expected to be much more flexible than EAC-truncated DGTD methods since the truncation surface can be any kind of shape. Numerical results demonstrate the accuracy and applicability of the proposed method in various scattering scenarios.

II. Formulation

A. DGTD Formulation

Let Ω denote the computation domain enclosing a scatterer with permittivity $\epsilon(\mathbf{r})$ and permeability $\mu(\mathbf{r})$. The scatterer resides in a background medium with permittivity ϵ_0 and permeability μ_0 and is illuminated by an incident electromagnetic field $\{\mathbf{E}^{\rm inc}(\mathbf{r},t),\mathbf{H}^{\rm inc}(\mathbf{r},t)\}$, $\mathbf{r}\in\mathbb{R}^3$ and $t\in[0,\infty)$. To facilitate the solution of the transient scattering problem, i.e., to find the electromagnetic fields $\{\mathbf{E}(\mathbf{r},t),\mathbf{H}(\mathbf{r},t)\}$ in Ω, using the DGTDBI method (Fig. 1): (i) Ω is assumed to be terminated by surface $\partial\Omega$. (ii) Ω is divided into two regions: Total and scattered field (TF/SF) regions. Note that the SF region surrounds the TF region and the surface between them is denoted by $\partial\Omega^{\rm T}$. (iii) $\partial\Omega^{\rm T}$ is assumed to coincide with or be enclosed by the Huygens' surface $\partial\Gamma$. Next, Ω is discretized into N number of non-overlapping tetrahedral elements Ω_i with boundary $\partial\Omega_i$, $i=1,\dots N$. In each Ω_i, $\mathbf{E}$ and $\mathbf{H}$ are approximated as

$$\mathbf{E}_i(\mathbf{r},t)=\sum_{k=1}^{d_i^{\rm e}} f_{i,k}^{\rm e}(t)\boldsymbol{\Psi}_{i,k}^{\rm e}(\mathbf{r})$$
$$\mathbf{H}_i(\mathbf{r},t)=\sum_{l=1}^{d_i^{\rm h}} f_{i,l}^{\rm h}(t)\boldsymbol{\Psi}_{i,l}^{\rm h}(\mathbf{r}). \tag{1}$$

Here, $\boldsymbol{\Psi}_{i,l}^{\rm p}$, ${\rm p}\in\{{\rm e},{\rm h}\}$, denote the independent edge vector basis functions and $d_i^{\rm p}$ and $f_{i,l}^{\rm p}$ are their numbers and unknown time dependent coefficients, respectively. Applying the DG testing to (source-free) Maxwell curl equations in Ω_i yields

$$\begin{aligned}&\int_{\Omega_i}\boldsymbol{\Psi}_{i,k}^{\rm e}\cdot[\epsilon_i\partial_t\mathbf{E}_i-\nabla\times\mathbf{H}_i]d\mathbf{r}\\&\quad=\sum_{m=1}^{4}\int_{\partial\Omega_{i,m}}\boldsymbol{\Psi}_{i,k}^{\rm e}\cdot[\hat{\mathbf{n}}_{i,m}\times(\mathbf{H}_m^*-\mathbf{H}_i)]\,d\mathbf{r}\\&\int_{\Omega_i}\boldsymbol{\Psi}_{i,l}^{\rm h}\cdot[\mu_i\partial_t\mathbf{H}_i+\nabla\times\mathbf{E}_i]d\mathbf{r}\\&\quad=\sum_{m=1}^{4}\int_{\partial\Omega_{i,m}}\boldsymbol{\Psi}_{i,l}^{\rm h}\cdot[\hat{\mathbf{n}}_{i,m}\times(\mathbf{E}_i-\mathbf{E}_m^*)]\,d\mathbf{r}.\end{aligned}\tag{2}$$

Here, ϵ_i and μ_i are the permittivity and the permeability assumed constant in Ω_i, $\partial\Omega_{i,m}$ is the $m^{\rm th}$ facet of the boundary $\partial\Omega_i$, $\hat{\mathbf{n}}_{i,m}$ is the unit outward normal to $\partial\Omega_{i,m}$, and $\hat{\mathbf{n}}_{i,m}\times\mathbf{H}_m^*$ and $\hat{\mathbf{n}}_{i,m}\times\mathbf{E}_m^*$ are the numerical fluxes. Solving the Riemann problem under the Rankine-Hugoniot condition yields an expression for the upwind flux [12]–[17]:

$$\begin{aligned}\hat{\mathbf{n}}_{i,m}\times\mathbf{H}_m^*&=\hat{\mathbf{n}}_{i,m}\times\frac{Z_i\mathbf{H}_i+\hat{\mathbf{n}}_{i,m}\times\mathbf{E}_i+\tilde{Z}\tilde{\mathbf{H}}-\hat{\mathbf{n}}_{i,m}\times\tilde{\mathbf{E}}}{Z_i+\tilde{Z}}\\\hat{\mathbf{n}}_{i,m}\times\mathbf{E}_m^*&=\hat{\mathbf{n}}_{i,m}\times\frac{Y_i\mathbf{E}_i-\hat{\mathbf{n}}_{i,m}\times\mathbf{H}_i+\tilde{Y}\tilde{\mathbf{E}}+\hat{\mathbf{n}}_{i,m}\times\tilde{\mathbf{H}}}{Y_i+\tilde{Y}}.\end{aligned}\tag{3}$$

Here $Z_i=\sqrt{\mu_i/\epsilon_i}$ and $Y_i=1/Z_i$ are the wave impedance and admittance in Ω_i. It is clear from (3) that the numerical fluxes consist of two parts: (1) Outgoing flux involving the fields $\mathbf{E}_i$ and $\mathbf{H}_i$ in Ω_i. Equation (2) Incoming flux involving the fields $\tilde{\mathbf{E}}$ and $\tilde{\mathbf{H}}$ that are "external" to Ω_i. The incoming flux is used to (i) establish the "connectivity" between fields in Ω_i and other elements "touching" $\partial\Omega_{i,m}$, (ii) to enforce the boundary condition on $\partial\Omega$, and (iii) to introduce the incident field $\{\mathbf{E}^{\rm inc},\mathbf{H}^{\rm inc}\}$ in $\partial\Omega_{\rm T}$ [17]. Accordingly, $\tilde{\mathbf{E}}$ and $\tilde{\mathbf{H}}$ in (3) are selected/computed as

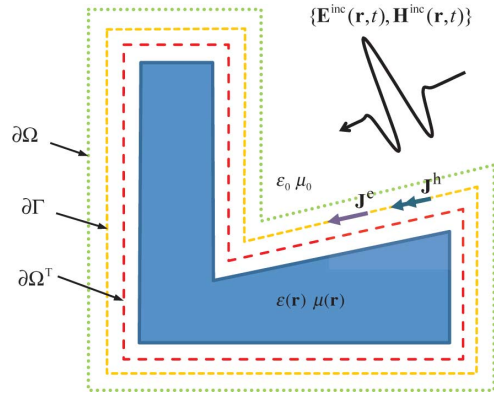

Fig. 1. Illustration of the scatterer, computation domain boundary $\partial\Omega$, Huygens' surface $\partial\Gamma$, and TF/SF surface $\partial\Omega^{\rm T}$, and the excitation.

$$\tilde{\mathbf{E}}=\begin{cases}\mathbf{E}_{i,m}^{\partial\Omega} & \partial\Omega_{i,m}\in\partial\Omega\\ \mathbf{E}_j\pm\mathbf{E}_{i,m}^{\rm inc} & \partial\Omega_{i,m}\in\partial\Omega^{\rm T}\\ \mathbf{E}_j & \text{else}\end{cases}$$
$$\tilde{\mathbf{H}}=\begin{cases}\mathbf{H}_{i,m}^{\partial\Omega} & \partial\Omega_{i,m}\in\partial\Omega\\ \mathbf{H}_j\pm\mathbf{H}_{i,m}^{\rm inc} & \partial\Omega_{i,m}\in\partial\Omega^{\rm T}\\ \mathbf{H}_j & \text{else}\end{cases}\tag{4}$$

depending on the location of $\partial\Omega_{i,m}$. Here, j is the index of the element that neighbors element i on the facet $\partial\Omega_{i,m}$, $\mathbf{E}_{i,m}^{\partial\Omega}$ and $\mathbf{H}_{i,m}^{\partial\Omega}$ are the fields enforced on $\partial\Omega_{i,m}\in\partial\Omega$, and $\mathbf{E}_{i,m}^{\rm inc}$ and $\mathbf{H}_{i,m}^{\rm inc}$ are the incident fields computed on $\partial\Omega_{i,m}\in\partial\Omega^{\rm T}$, and finally, '+'/'−' sign should be selected if Ω_i is in the TF/SF region. Similarly, $\tilde{Z}$ and $\tilde{Y}$ are

$$\tilde{Z}=\begin{cases}Z_0 & \partial\Omega_{i,m}\in\partial\Omega\\ Z_j & \text{else}\end{cases}$$
$$\tilde{Y}=\begin{cases}Y_0 & \partial\Omega_{i,m}\in\partial\Omega\\ Y_j & \text{else}\end{cases}\tag{5}$$

where $Z_0=\sqrt{\mu_0/\epsilon_0}$ and $Y_0=1/Z_0$ are the wave impedance and admittance in the background medium.

B. TDBI Formulation

Boundary fields $\mathbf{E}_{i,m}^{\partial\Omega}$ and $\mathbf{H}_{i,m}^{\partial\Omega}$ on $\partial\Omega_{i,m}\in\partial\Omega$ are computed using the TDBI method as described next. Let the Huygens' surface $\partial\Gamma$ be discretized by triangular facets $\partial\Omega_{i',m'}$, where i' runs over the indices of elements that are outside the volume enclosed by $\partial\Gamma$ and have at least three nodes residing on $\partial\Gamma$, and m' runs over the indices of each element's facets that are described by these nodes. On the surface mesh described by $\partial\Omega_{i',m'}$, one can introduce (equivalent) electric and magnetic surface currents, $\mathbf{J}_{i',m'}^{\rm h}(\mathbf{r},t)$ and $\mathbf{J}_{i',m'}^{\rm e}(\mathbf{r},t)$ [10], [11]:

$$\mathbf{J}_{i',m'}^{\rm h}(\mathbf{r},t)=\sum_{l'=1}^{d_{i'}^{\rm h}} f_{i',l'}^{\rm h}(t)\hat{\mathbf{n}}_{i',m'}(\mathbf{r})\times\boldsymbol{\Psi}_{i',l'}^{\rm h}(\mathbf{r})$$
$$\mathbf{J}_{i',m'}^{\rm e}(\mathbf{r},t)=-\sum_{k'=1}^{d_{i'}^{\rm e}} f_{i',k'}^{\rm e}(t)\hat{\mathbf{n}}_{i',m'}(\mathbf{r})\times\boldsymbol{\Psi}_{i',k'}^{\rm e}(\mathbf{r}).\tag{6}$$

The boundary fields $\mathbf{E}^{\partial\Omega}_{i,m}$ and $\mathbf{H}^{\partial\Omega}_{i,m}$ are then constructed using currents $\mathbf{J}^{\mathrm{h}}_{i',m'}$ and $\mathbf{J}^{\mathrm{e}}_{i',m'}$[10], [11]:

$$\begin{aligned}\mathbf{E}^{\partial\Omega}_{i,m}(\mathbf{r},t) &= \sum_{i'}\sum_{m'}[\mu_0\mathcal{L}_{i',m'}(\mathbf{J}^{\mathrm{h}}_{i',m'}) - \mathcal{K}_{i',m'}(\mathbf{J}^{\mathrm{e}}_{i',m'})]\\ \mathbf{H}^{\partial\Omega}_{i,m}(\mathbf{r},t) &= \sum_{i'}\sum_{m'}[\epsilon_0\mathcal{L}_{i',m'}(\mathbf{J}^{\mathrm{e}}_{i',m'}) + \mathcal{K}_{i',m'}(\mathbf{J}^{\mathrm{h}}_{i',m'})]. \quad (7)\end{aligned}$$

Here, the operators $\mathcal{L}_{i',m'}$ and $\mathcal{K}_{i',m'}$ are defined as

$$\begin{aligned}\mathcal{L}_{i',m'}(\mathbf{J}) &= -\frac{1}{4\pi}\int_{\partial\Omega_{i',m'}}\frac{\partial_t\mathbf{J}\left(\mathbf{r}',t-\frac{R}{c_0}\right)}{R}d\mathbf{r}'\\ &\quad+\frac{c_0^2}{4\pi}\nabla\int_{\partial\Omega_{i',m'}}\int_0^{t-R/c_0}\frac{\nabla'\cdot\mathbf{J}(\mathbf{r}',t')}{R}dt'd\mathbf{r}'\\ \mathcal{K}_{i',m'}(\mathbf{J}) &= \frac{1}{4\pi}\nabla\times\int_{\partial\Omega_{i',m'}}\frac{\mathbf{J}\left(\mathbf{r}',t-\frac{R}{c_0}\right)}{R}d\mathbf{r}' \quad (8)\end{aligned}$$

where $R=|\mathbf{r}-\mathbf{r}'|$ is the distance between the integration point $\mathbf{r}'\in\partial\Omega_{i',m'}$ and the observation point $\mathbf{r}$ and $c_0=1/\sqrt{\epsilon_0\mu_0}$ is the speed of light in the background medium.

C. Final System of Equations

Inserting (1), (3), and (7) into (2) yields a linear semi-discrete coupled system of equations:

$$\begin{aligned}\epsilon_i\bar{\mathbf{M}}^{\mathrm{e}}_i\partial_t\mathbf{e}_i &= [\bar{\mathbf{S}}^{\mathrm{eh}}_i-\bar{\mathbf{F}}^{\mathrm{eh}}_{ii}]\mathbf{h}_i+\bar{\mathbf{F}}^{\mathrm{ee}}_{ii}\mathbf{e}_i+\sum_j[\bar{\mathbf{F}}^{\mathrm{eh}}_{ij}\mathbf{h}_j-\bar{\mathbf{F}}^{\mathrm{ee}}_{ij}\mathbf{e}_j]\\ &\quad-\mathbf{t}^{\mathrm{ee}}_i+\mathbf{t}^{\mathrm{eh}}_i\mp\mathbf{b}^{\mathrm{ee}}_i\pm\mathbf{b}^{\mathrm{eh}}_i\\ \mu_i\bar{\mathbf{M}}^{\mathrm{h}}_i\partial_t\mathbf{h}_i &= [-\bar{\mathbf{S}}^{\mathrm{he}}_i+\bar{\mathbf{F}}^{\mathrm{he}}_{ii}]\mathbf{e}_i+\bar{\mathbf{F}}^{\mathrm{hh}}_{ii}\mathbf{h}_i-\sum_j[\bar{\mathbf{F}}^{\mathrm{he}}_{ij}\mathbf{e}_j+\bar{\mathbf{F}}^{\mathrm{hh}}_{ij}\mathbf{h}_j]\\ &\quad-\mathbf{t}^{\mathrm{hh}}_i-\mathbf{t}^{\mathrm{he}}_i\mp\mathbf{b}^{\mathrm{hh}}_i\mp\mathbf{b}^{\mathrm{he}}_i. \quad (9)\end{aligned}$$

Here, $\mathbf{e}_i$ and $\mathbf{h}_i$ are vectors that store the unknown coefficients $f^{\mathrm{e}}_{i,k}$ and $f^{\mathrm{h}}_{i,l}$, respectively, and the *non-zero* entries of the remaining matrices and vectors are

$$\begin{aligned}[\bar{\mathbf{M}}^{\mathrm{p}}_i]_{kl} &= \int_{\Omega_i}\boldsymbol{\Psi}^{\mathrm{p}}_{i,k}\cdot\boldsymbol{\Psi}^{\mathrm{p}}_{i,l}d\mathbf{r},\ \ [\bar{\mathbf{S}}^{\mathrm{p}\tilde{\mathrm{p}}}_i]_{kl}=\int_{\Omega_i}\boldsymbol{\Psi}^{\mathrm{p}}_{i,k}\cdot\nabla\times\boldsymbol{\Psi}^{\tilde{\mathrm{p}}}_{i,l}d\mathbf{r}\\ [\bar{\mathbf{F}}^{\mathrm{pp}}_{ii}]_{kl} &= \sum_{m=1}^{4}A^{\mathrm{p}}_m\int_{\partial\Omega_{i,m}}\boldsymbol{\Psi}^{\mathrm{p}}_{i,k}\cdot\hat{\mathbf{n}}_{i,m}\times(\hat{\mathbf{n}}_{i,m}\times\boldsymbol{\Psi}^{\mathrm{p}}_{i,l})d\mathbf{r}\\ [\bar{\mathbf{F}}^{\mathrm{p}\tilde{\mathrm{p}}}_{ii}]_{kl} &= \sum_{m=1}^{4}B^{\mathrm{p}}_m\int_{\Omega_{i,m}}\boldsymbol{\Psi}^{\mathrm{p}}_{i,k}\cdot\hat{\mathbf{n}}_{i,m}\times\boldsymbol{\Psi}^{\tilde{\mathrm{p}}}_{i,l}d\mathbf{r}\\ [\bar{\mathbf{F}}^{\mathrm{pp}}_{ij}]_{kl} &= A^{\mathrm{p}}_m\int_{\partial\Omega_{i,m}}\boldsymbol{\Psi}^{\mathrm{p}}_{i,k}\cdot\hat{\mathbf{n}}_{i,m}\times(\hat{\mathbf{n}}_{i,m}\times\boldsymbol{\Psi}^{\mathrm{p}}_{j,l})d\mathbf{r}\\ [\bar{\mathbf{F}}^{\mathrm{p}\tilde{\mathrm{p}}}_{ij}]_{kl} &= B^{\mathrm{p}}_m\int_{\partial\Omega_{i,m}}\boldsymbol{\Psi}^{\mathrm{p}}_{i,k}\cdot\hat{\mathbf{n}}_{i,m}\times\boldsymbol{\Psi}^{\tilde{\mathrm{p}}}_{j,l}d\mathbf{r}\\ [\mathbf{b}^{\mathrm{pp}}_i]_k &= \sum_m A^{\mathrm{p}}_m\int_{\partial\Omega_{i,m}\in\partial\Omega^{\mathrm{T}}}\boldsymbol{\Psi}^{\mathrm{p}}_{i,k}\cdot\hat{\mathbf{n}}_{i,m}\times(\hat{\mathbf{n}}_{i,m}\times\mathbf{b}^{\mathrm{p}}_{i,m})d\mathbf{r}\\ [\mathbf{b}^{\mathrm{p}\tilde{\mathrm{p}}}_i]_k &= \sum_m B^{\mathrm{p}}_m\int_{\partial\Omega_{i,m}\in\partial\Omega^{\mathrm{T}}}\boldsymbol{\Psi}^{\mathrm{p}}_{i,k}\cdot\hat{\mathbf{n}}_{i,m}\times\mathbf{b}^{\tilde{\mathrm{p}}}_{i,m}d\mathbf{r}\\ [\mathbf{t}^{\mathrm{pp}}_i]_k &= \sum_m A^{\mathrm{p}}_m\int_{\partial\Omega_{i,m}\in\partial\Omega}\boldsymbol{\Psi}^{\mathrm{p}}_{i,k}\cdot\hat{\mathbf{n}}_{i,m}\times(\hat{\mathbf{n}}_{i,m}\times\mathbf{i}^{\mathrm{p}}_{i,m})d\mathbf{r}\\ [\mathbf{t}^{\mathrm{p}\tilde{\mathrm{p}}}_i]_k &= \sum_m B^{\mathrm{p}}_m\int_{\partial\Omega_{i,m}\in\partial\Omega}\boldsymbol{\Psi}^{\mathrm{p}}_{i,k}\cdot\hat{\mathbf{n}}_{i,m}\times\mathbf{i}^{\tilde{\mathrm{p}}}_{i,m}d\mathbf{r}. \quad (10)\end{aligned}$$

In (10), $\mathrm{p}\in\{\mathrm{e},\mathrm{h}\}$, $\tilde{\mathrm{p}}=\mathrm{h}$ for $\mathrm{p}=\mathrm{e}$ and $\tilde{\mathrm{p}}=\mathrm{e}$ for $\mathrm{p}=\mathrm{h}$, $A^{\mathrm{e}}_m=1/(Z_i+\tilde{Z})$, $A^{\mathrm{h}}_m=1/(Y_i+\tilde{Y})$, $B^{\mathrm{e}}_m=\tilde{Z}/(Z_i+\tilde{Z})$, $B^{\mathrm{h}}_m=\tilde{Y}/(Y_i+\tilde{Y})$, $\mathbf{b}^{\mathrm{e}}_{i,m}=\mathbf{E}^{\mathrm{inc}}_{i,m}$, $\mathbf{b}^{\mathrm{h}}_{i,m}=\mathbf{H}^{\mathrm{inc}}_{i,m}$, and

$$\begin{aligned}\mathbf{i}^{\mathrm{e}}_{i,m} &= \sum_{i'}\sum_{m'}\left\{\sum_{l'=1}^{d^{\mathrm{h}}_{i'}}\mu_0\mathcal{L}_{i',m'}(f^{\mathrm{h}}_{i',l'}\hat{\mathbf{n}}_{i',m'}\times\boldsymbol{\Psi}^{\mathrm{h}}_{i',l'})\right.\\ &\quad\left.+\sum_{k'=1}^{d^{\mathrm{e}}_{i'}}\mathcal{K}_{i',m'}(f^{\mathrm{e}}_{i',k'}\hat{\mathbf{n}}_{i',m'}\times\boldsymbol{\Psi}^{\mathrm{e}}_{i',k'})\right\}\\ \mathbf{i}^{\mathrm{h}}_{i,m} &= \sum_{i'}\sum_{m'}\left\{\sum_{l'=1}^{d^{\mathrm{h}}_{i'}}\mathcal{K}_{i',m'}(f^{\mathrm{h}}_{i',l'}\hat{\mathbf{n}}_{i',m'}\times\boldsymbol{\Psi}^{\mathrm{h}}_{i',l'})\right.\\ &\quad\left.-\sum_{k'=1}^{d^{\mathrm{e}}_{i'}}\epsilon_0\mathcal{L}_{i',m'}(f^{\mathrm{e}}_{i',k'}\hat{\mathbf{n}}_{i',m'}\times\boldsymbol{\Psi}^{\mathrm{e}}_{i',k'})\right\}. \quad (11)\end{aligned}$$

D. Comments and Extensions

Several comments about the formulations of the DGTD and the TDBI methods in Sections II-A and II-B, and the final system of equations in Section II-C are in order:

On spatial discretization Basis functions $\boldsymbol{\Psi}^{\mathrm{e}}_{i,k}$ and $\boldsymbol{\Psi}^{\mathrm{h}}_{i,l}$ in expansion (1) are curl-confirming functions. Note that this makes functions $\hat{\mathbf{n}}_{i',m'}\times\boldsymbol{\Psi}^{\mathrm{e}}_{i',k'}$ and $\hat{\mathbf{n}}_{i',m'}\times\boldsymbol{\Psi}^{\mathrm{h}}_{i',l'}$ in expansion (6) divergence-conforming [15]. Let p represent the order of these expansions. Then, the DGTD scheme has an optimal $O(h^{p+1})$ convergence rate [13]–[16]. Here, h represents the edge size. Numerical experiments presented in [21], [22] demonstrate that TDBI scheme is expected to have a higher-order spatial convergence. Consequently, the DGTDBI scheme is higher-order in spatial discretization. Note that theoretical error estimates for three dimensional integral equations are yet to be developed [23].

On temporal discretization The semi-discrete system of equations in (9) is numerically integrated in time to obtain the samples of $\mathbf{e}_i$ and $\mathbf{h}_i$. Let Δt_{DG} represent the time step of the integration scheme used. To ensure stability, Δt_{DG} should satisfy a CFL-like condition that depends on the order and type of spatial discretization and time integration schemes as described in detail in [12]–[16]. On the other hand, TDBI scheme's time step, denoted by Δt_{BI}, is only required to resolve the maximum frequency of the excitation independent from the spatial discretization [19], [20]. In a typical scenario $\Delta t_{\mathrm{BI}}\gg\Delta t_{\mathrm{DG}}$; therefore, if one uses a single time step for the hybrid DGTDBI scheme and sets it to Δt_{DG}, TDBI scheme's computational requirements will increase significantly. Consequently, spatially discretized retarded-time surface integrals $\mathbf{i}^{\mathrm{p}}_{i,m}$ are sampled at $k\Delta t_{\mathrm{BI}}$ requiring computation of $f^{\mathrm{p}}_{i',l'}(k\Delta t_{\mathrm{BI}}-R/c_0)$. But during marching their samples at $k\Delta t_{\mathrm{DG}}$, i.e., $f^{\mathrm{p}}_{i',l'}(l\Delta t_{\mathrm{DG}})$, are available. Therefore, an interpolation scheme is needed to compute $f^{\mathrm{p}}_{i',l'}(k\Delta t_{\mathrm{BI}}-R/c_0)$ from $f^{\mathrm{p}}_{i',l'}(l\Delta t_{\mathrm{DG}})$. From the opposite side, only samples $\mathbf{i}^{\mathrm{p}}_{i,m}(k\Delta t_{\mathrm{BI}})$ are available during time marching. But time-integration scheme requires samples $\mathbf{t}^{\mathrm{pp}}_i(l\Delta t_{\mathrm{DG}})$ and $\mathbf{t}^{\mathrm{p}\tilde{\mathrm{p}}}_i(l\Delta t_{\mathrm{DG}})$. Therefore an interpolation scheme is needed to compute them from $\mathbf{i}^{\mathrm{p}}_{i,m}(k\Delta t_{\mathrm{BI}})$. Both interpolation steps are carried out using shifted higher-order Lagrange polynomials [19], [20]. Also, time derivative in operator $\mathcal{L}_{i',m'}$ is moved onto this interpolation function. It should also be noted here that, to maintain the explicitness of the time marching, which is one of the main advantages of DGTD scheme over classical finite element methods, the minimum distance between any two points on $\partial\Gamma$ and $\partial\Omega$ has to be larger than $c_0\Delta t_{\mathrm{BI}}$.

On applicability For the simplicity of presentation, the DGTD formulation in Section II-A is carried out for an isotropic scatterer. It can easily be extended to account for dispersive and/or anisotropic

TABLE I
l_{avg}(m), Δt_{DG}(ps), Δt_{BI}(ps), DURATION (ns), CPU TIME (m), AND MEMORY (GB) FOR NUMERICAL EXAMPLES

$\cdots$	l_{avg}	Δt_{DG}	Δt_{BI}	Duration	CPU Time	Memory
3-Sph	0.016	1.39	21.3	27.8	63.7	5.41
U-PEC	0.015	1.54	23.3	23.7	38.6	4.12
U-Diel	0.012	1.28	23.3	22.8	43.4	4.21
Plas-Sph	0.016	1.25	20.1	18.75	31.2	3.08

scatterers as described in [7]. Similarly, the TDBI formulation in Section II-B is carried out for a single scatterer. It can easily be extended to account for local truncation of domains each of which is defined around a disconnected scatterer. Examples of scattering scenarios requiring these extensions can be found in Section III.

On computational requirements Depending on the shape of the scatterer, the evaluation of $\mathbf{t}_i^{\text{pp}}$'s non-zero elements for all time samples might be computationally dominant over the other operations during time marching. This can be accelerated for example using time-domain adaptive integral [19], [20] or plane wave time-domain [10], [11] methods.

III. NUMERICAL RESULTS

In this section, numerical results that demonstrate the accuracy of the proposed DGTDBI method are presented. In all scattering scenarios considered here, the excitation is a plane wave with electric field $\mathbf{E}^{\text{inc}}(\mathbf{r},t) = \hat{\mathbf{p}}E_0 G(t - \hat{\mathbf{k}}\cdot\mathbf{r}/c_0)$, where $\hat{\mathbf{p}} = \hat{\mathbf{x}}$ is the polarization, $\hat{\mathbf{k}} = \hat{\mathbf{z}}$ is the direction of propagation, $E_0 = 1$ V/m is the amplitude, and $G(t) = \exp(-[t-t_0]^2/\tau_m^2)\cos(2\pi f_m[t-t_0])$ is a Gaussian pulse with modulation frequency f_m, delay t_0, and duration τ_m. The Huygens' surface coincides with the TF/SF boundaries for all examples. The time-integrator is the explicit fourth-order Runge Kutta scheme [13] even though other explicit schemes, such as the well-known Adam's Bashfort or more recently developed Rokhlin-Glaser schemes [18] can be used. Basis functions $\mathbf{\Psi}_{i,k}^{\text{e}}$ and $\mathbf{\Psi}_{i,l}^{\text{h}}$ are "mixed-order" constant-tangential/linear-normal (CT/LN) functions resulting in $d_i^{\text{e}} = 6$ and $d_i^{\text{h}} = 6$. Linear Lagrange polynomial is used to compute the temporal interpolations described in Section II-D. Computational requirements, duration of time marching, average edge length of the spatial discretization l_{avg} and time steps Δt_{BI} and Δt_{DG} used in each numerical example are provided in Table I. All simulations are carried out on a single-core Intel(R) Core(TM) i7–3770 computer

A. Cluster of Spheres

In this example, the scatterer is a cluster of three perfect electrically conducting (PEC) spheres residing in free space Fig. 2. Use of the TDBI approach allows the computation domain to be defined in terms of three equally sized domains, each of which encloses one of the spheres. Disconnected spherical boundaries of the these domains and the Huygens' surfaces are located 0.03 m and 0.015 m away from the sphere surfaces Fig. 2. For the first simulation, the cluster is excited with a plane wave with parameters $f_m = 500$ MHz, $t_0 = 13.66$ ns, and $\tau_m = 2.6$ ns. During the simulation, the transient scattered electric near field computed at the origin is recorded. Fig. 3 compares this field to that computed using a time-domain integral equation (TDIE) solver [19], [20]. Results agree well.

For the second simulation, $\tau_m = 0.65$ ns while other excitation parameters are kept the same. After the time-domain simulation, radar-cross-section (RCS) of the cluster is computed from the Fourier-transformed currents on the Huygens' surfaces. Figs. 4 and 5 plot the RCS on the xy- and xz- planes computed at 2.53 MHz and 1.003 GHz, respectively. Results agree very well with those obtained from the solution of an in-house method of moments (MoM) solver. These two figures clearly demonstrate that the "absorption" enforced by the TDBI approach is accurate even at low frequencies.

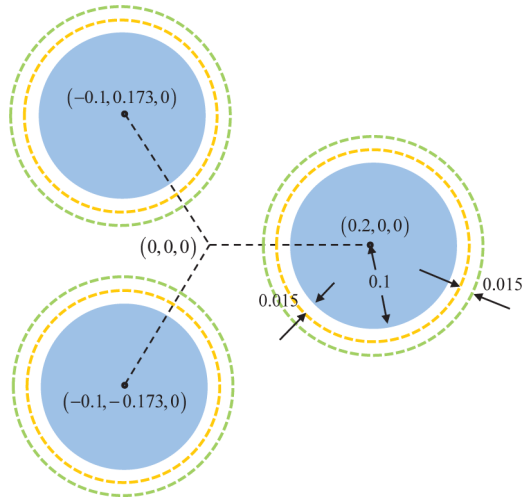

Fig. 2. Cluster of three PEC spheres. All dimensions are in meters.

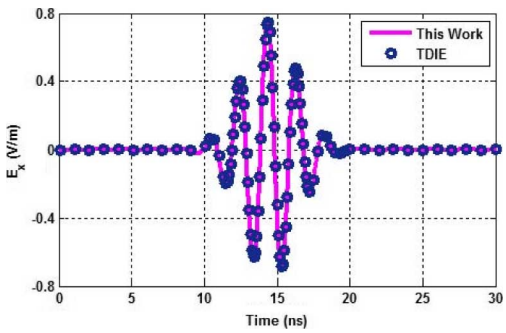

Fig. 3. Transient scattered electric field computed at the origin of cluster of PEC spheres.

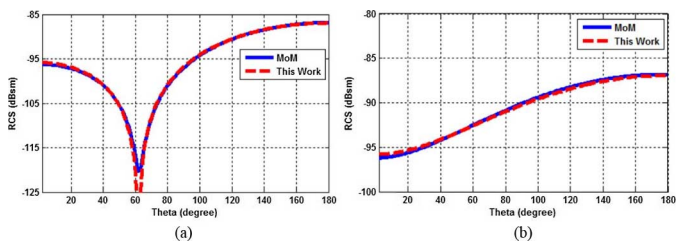

Fig. 4. RCS on (a) xy- and (b) xz- planes computed at 2.53 MHz from the solutions of the DGTDBI method and MoM.

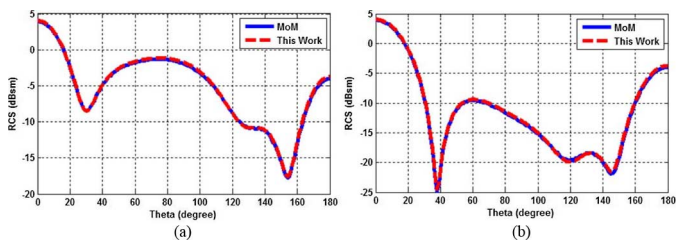

Fig. 5. RCS on (a) xy- and (b) xz- planes computed at 1.003 GHz from the solutions of the DGTDBI method and MoM.

B. U-Shape Scatterer

The second scatterer is a U-shape object residing in free space (Fig. 6). The boundary of the computation domain and the Huygens'

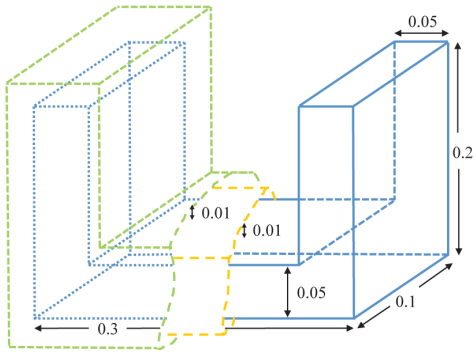

Fig. 6. U-shaped scatterer. All dimensions are in meters.

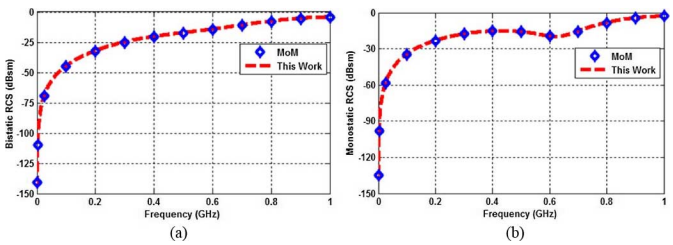

Fig. 7. The bistatic (a) and monostatic (b) RCS of the PEC U-shaped scatterer computed at a range of frequencies changing from 286.4 KHz to 1.0 GHz.

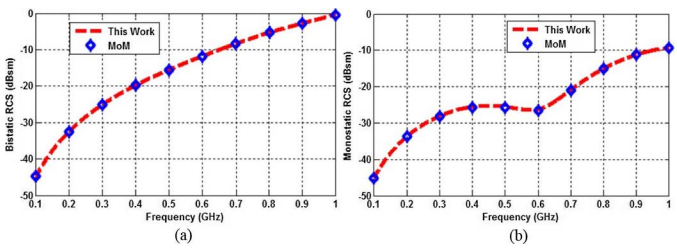

Fig. 8. The bistatic (a) and monostatic (b) RCS of the dielectric U-shaped scatterer computed at a range of frequencies changing from 100 MHz to 1.0 GHz.

surface conform to the shape of the scatterer and are located 0.02 m and 0.01 m away from its surface. The scatterer is excited with a plane wave with parameters $f_m = 500$ MHz, $t_0 = 13.66$ ns, and $\tau_m = 2.6$ ns. Two simulations are carried out: (i) The scatterer surface is PEC. (ii) The scatterer is a dielectric body with relative permittivity of 4.0. After the time-domain simulations, bistatic and monostatic RCS of the scatterers are computed from the Fourier-transformed currents on the Huygens' surfaces. Fig. 7(a) and (b) and Fig. 8(a) and (b) plot the bistatic and monostatic RCS of the PEC and dielectric scatterers computed at a wide range of frequencies, respectively. Figures clearly demonstrate that the results agree very well with those obtained from the solution of an MoM solver further verifying the accuracy and also low-frequency absorbing capability of the DGTDBI method. Additionally, Fig. 9(a) and (b) compare the RCS of the PEC scatterer on the xz- and yz-planes computed at 1 GHz to those obtained by the same DGTD, which uses ABC instead of TDBI. It is clearly shown that ABC is not accurate for this structure.

C. Plasma Coated PEC Sphere

In the last example, the scatterer is a PEC sphere coated with a layer of (magnetized) plasma. The radius of the sphere and the thickness of the layer are 0.1 m and 0.05 m, respectively. The scatterer resides in free space and centered at the origin. The computation domain and the Huygens' surface are located 0.03 m, and 0.015 m away from the exterior surface of the plasma layer.

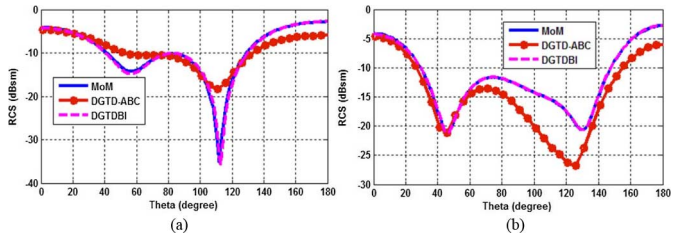

Fig. 9. The calculated RCS in xoz (a) and yoz (b) planes with DGTDBI method and its comparisons from MoM and DGTD-ABC at 1.00013 GHz.

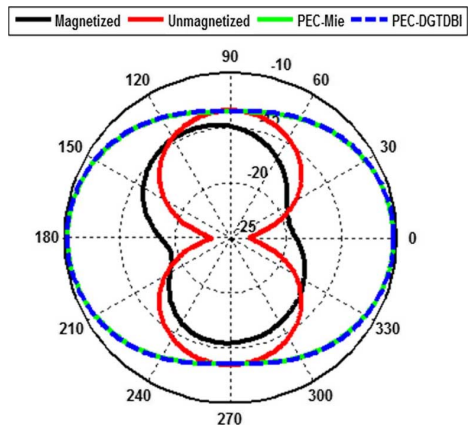

Fig. 10. The RCS (in dBsm) of the plasma coated PEC sphere on the xy-plane computed at 1000.29 MHz.

When a static magnetic field is applied, the plasma layer becomes a dispersive anisotropic gyroelectric medium with a full permittivity tensor with both non-zero diagonal and off-diagonal elements [24]. To model the dispersive anisotropy of the plasma layer, an auxiliary differential equation that involves an auxiliary polarization vector $\mathbf{P}(\mathbf{r}, t)$ is introduced [7], [24]:

$$\partial_t \mathbf{P} + \upsilon_e \mathbf{P} = \epsilon_0 \omega_{P_e}^2 \mathbf{E} + \boldsymbol{\omega_{C_e}} \times \mathbf{P}. \tag{12}$$

Here, ω_{P_e} and υ_e denote the magnetized plasma and the electron collision frequencies, and $mmb\omega_{C_e} = (\omega_{C_e}^x, \omega_{C_e}^y, \omega_{C_e}^y)$ is the cyclotron frequency vector. Note that $\omega_{C_e}^x = \omega_{C_e}^y = \omega_{C_e}^z = 0$ when there is no biasing magnetic. The auxiliary polarization vector $\mathbf{P}$ is added to the Ampere's law equation and (12) and the updated Maxwell curl equations are solved together. Note that the numerical flux [see (2)] and the TDBI (see Section II-B) formulations remain unchanged. The discretization of the additional unknown $\mathbf{P}$ is carried out in the same way as $\mathbf{E}$ and $\mathbf{H}$ [see (1)].

The magnetized plasma coated PEC sphere is excited with a plane wave with parameters $f_m = 500$ MHz, $t_0 = 13.66$ ns, and $\tau_m = 2.6$ ns. Three scatterers are considered: (i) The permittivity of the layer is set to ϵ_0, i.e., the scatterer is only the PEC sphere. (ii) Plasma layer is assumed unmagnetized, i.e., $\omega_{C_e}^x = \omega_{C_e}^y = \omega_{C_e}^z = 0$. (iii) Plasma layer is assumed magnetized, i.e., $\omega_{C_e}^x = \omega_{C_e}^y = \omega_{C_e}^z = 2\pi \times 10^9$ rad/s. For scatterers (ii) and (iii), $\omega_{P_e} = 2.8\pi \times 10^9$ rad/s and $\upsilon_e = 2\pi \times 10^9$ rad/s. After the time domain simulations, the RCS of the scatterers on the xy plane is computed at 1000.29 MHz from the Fourier-transformed currents on the Huygens' surfaces. As shown in Fig. 10, the RCS of the three scatterers are quite different. One interesting observation is that the RCS is significantly reduced for scatterers (ii) and (iii), i.e., when the PEC sphere is coated with the plasma layer.

This phenomenon is termed "plasma stealth" and it can be explained by the fact that plasma "absorbs" electromagnetic waves. Also, it should be noted that the symmetry of the RCS pattern is broken for scatterer (iii), i.e., when a biasing magnetic field is imposed. For scatterer (iii), in addition to electric force, Lorentz force also exists; this makes the RCS non-symmetrical.

IV. Conclusion

A hybrid DGTDBI method is proposed for analyzing transient scattering penetrable scatterers. The radiation condition is rigorously enforced via the incoming numerical flux on the truncation domain boundary of the computation domain. The fields required by flux are computed using TDBI method from equivalent currents introduced on a Huygens' surface enclosing the scatters. The use of TDBI ensures that the truncation boundary is located very close to scatterer surface without any loss of accuracy. Additionally, it allows for locally truncated computation domains each of which is defined around a disconnected scatterer. These significantly reduce the number of DGTD elements discretizing volumes. Numerical results demonstrating the accuracy and the applicability of the hybrid DGTDBI in various scattering scenarios are presented.

References

[1] T. Hagstrom, T. Warburton, and D. Givoli, "Radiation boundary conditions for time-dependent waves based on complete plane wave expansions," *J. Comp. Appl. Math.*, vol. 234, pp. 1988–1995, Aug. 2010.

[2] K. Sirenko, M. Liu, and H. Bagci, "Incorporation of exact boundary conditions into a discontinuous Galerkin finite element method for accurately solving 2D time-dependent Maxwell equations," *IEEE Trans. Antennas Propag.*, vol. 61, no. 1, pp. 472–477, Jan. 2013.

[3] G. Mur, "Absorbing boundary conditions for the finite-difference approximation of time-domain electromagnetic field equations," *IEEE Trans. Electromagn. Compat.*, vol. 23, no. 4, pp. 377–382, Apr. 1981.

[4] R. L. Higdon, "Absorbing boundary conditions for difference approximations to the multidimensional wave equation," *Math. Comput.*, vol. 47, pp. 437–459, 1986.

[5] J. P. Berenger, "Perfectly matched layer for the absorption of electromagnetic waves," *J. Comput. Phys.*, vol. 114, no. 2, pp. 185–200, 1994.

[6] S. D. Gedney, "An anisotropic perfectly matched layer-absorbing medium for the truncation of FDTD lattices," *IEEE Trans. Antennas Propag.*, vol. 44, no. 12, pp. 1630–1639, Dec. 1996.

[7] S. D. Gedney, J. C. Yong, T. C. Kramer, and J. A. Roden, "A discontinuous Galerkin finite element time-domain method modeling of dispersive media," *IEEE Trans. Antennas Propag.*, vol. 60, no. 4, pp. 1969–1977, Apr. 2012.

[8] S. D. Gedney and B. Zhao, "An auxiliary differential equation formulation for the complex-frequency shifted PML," *IEEE Trans. Antennas Propag.*, vol. 58, no. 3, pp. 838–847, Mar. 2010.

[9] S. Abarbanel, D. Gottlieb, and J. S. Hesthaven, "Long time behavior of the perfectly matched layer equations in computational electromagnetics," *J. Sci. Comput.*, vol. 17, no. 1-4, pp. 405–422, Dec. 2002.

[10] D. Jiao, A. A. Ergin, B. Shanker, E. Michielssen, and J. M. Jin, "A fast higher-order time-domain finite element-boundary integral method for 3-D electromagnetic scattering analysis," *IEEE Trans. Antennas Propag.*, vol. 50, no. 9, pp. 1192–1202, Sep. 2002.

[11] B. Shanker, M. Y. Lu, A. A. Ergin, and E. Michielssen, "Plane-wave time-domain acclerated radiation boundary kernels for FDTD analysis of 3-D electromagnetic phenomena," *IEEE Trans. Antennas Propag.*, vol. 53, no. 11, pp. 3704–3716, Nov. 2005.

[12] S. D. Gedney, C. Luo, J. A. Roden, R. D. Crawford, B. Guernsey, J. A. Miller, T. Kramer, and E. W. Lucas, "The discontinuous Galerkin finite-element time-domain method solution of Maxwell's equations," *J. Appl. Comput. Electromagn. Soc.*, vol. 24, no. 2, pp. 129–142, Apr. 2009.

[13] J. S. Hesthaven and T. Warburton, *Nodal Discontinuous Galerkin Methods*. Berlin: Springer, 2008.

[14] S. Dosopoulos and J. F. Lee, "Interior penalty discontinuous Galerkin method for the time-domain Maxwell's equations," *IEEE Trans. Magn.*, vol. 46, no. 8, pp. 3512–3515, Aug. 2010.

[15] S. Dosopoulos and J.-F. Lee, "Interconnect and lumped elements modeling in interior penalty discontinuous Galerkin time-domain methods," *J. Comput. Phys.*, vol. 229, no. 22, pp. 8521–8536, Nov. 2010.

[16] L. Fezoui, S. Lanteri, S. Lohrengel, and S. Piperno, "Convergence and stability of a discontinuous Galerkin time-domain method for the 3D heterogeneous Maxwell equations on unstructured meshes," *ESAIM: Math. Model. Numer. Anal.*, vol. 39, no. 6, pp. 1149–1176, Nov. 2005.

[17] J. Alvarez, L. D. Angulo, M. F. Pantoja, A. R. Bretones, and S. G. Garcia, "Source and boundary implementation in vector and scalar DGTD," *IEEE Trans. Antennas Propag.*, vol. 58, no. 6, pp. 1997–2003, Jun. 2010.

[18] M. Liu, K. Sirenko, and H. Bagci, "An efficient discontinuous Galerkin finite element method for highly accurate solution of Maxwell equations," *IEEE Trans. Antennas Propag.*, vol. 60, no. 8, pp. 3992–3998, Aug. 2012.

[19] A. E. Yilmaz, J.-M. Jin, and E. Michielssen, "Time domain adaptive integral method for surface integral equations," *IEEE Trans. Antennas Propag.*, vol. 52, no. 10, pp. 2692–2708, Oct. 2004.

[20] H. Bagci, A. E. Yilmaz, J.-M. Jin, and E. Michielssen, "Fast and rigorous analysis of EMC/EMI phenomena on electrically large and complex cable-loaded structures," *IEEE Trans. Electromagn. Comp.*, vol. 49, no. 2, pp. 361–381, May 2007.

[21] A. F. Peterson, "Observed baseline convergence rates and superconvergence in the scattering cross section obtained from numerical solutions of the MFIE," *IEEE Trans. Antennas Propag.*, vol. 56, no. 11, pp. 3510–3515, Nov. 2008.

[22] K. C. Donepudi, J.-M. Jin, and W. C. Chew, "A higher order multilevel fast multipole algorithm for scattering from mixed conducting/dielectric bodies," *IEEE Trans. Antennas Propag.*, vol. 51, no. 10, pp. 2814–2821, Oct. 2003.

[23] C. P. Davis and K. F. Warnick, "High-order convergence with a low-order discretization of the 2-D MFIE," *IEEE Antennas Wireless Propag. Lett.*, vol. 3, no. 1, pp. 355–358, Dec. 2004.

[24] F. Hunsberger, R. Luebbers, and K. Kunz, "Finite-difference time-domain analysis of gyrotropic media-I: magnetized plasma," *IEEE Trans. Antennas Propag.*, vol. 40, no. 12, pp. 1489–1495, Dec. 1992.